

# Chiral Phonons in Biocrystals

**Won Jin Choi**

University of Michigan <https://orcid.org/0000-0001-6303-8899>

**Keiichi Yano**

University of Michigan

**Minjeong Cha**

University of Michigan

**Felippe Colombari**

Brazilian Biorenewables National Laboratory

**Yichun Wang**

University of Notre Dame

**Sang Hyun Lee**

University of Michigan

**John Kruger**

Michigan State University

**Andre de Moura**

Federal University of São Carlos <https://orcid.org/0000-0003-1974-4803>

**Nicholas A Kotov** (✉ [kotov@umich.edu](mailto:kotov@umich.edu))

University of Michigan <https://orcid.org/0000-0002-6864-5804>

---

## Article

**Keywords:** chiral phonons, biocrystals, materials science, nanoscience, technology

**Posted Date:** March 1st, 2021

**DOI:** <https://doi.org/10.21203/rs.3.rs-248321/v1>

**License:**   This work is licensed under a Creative Commons Attribution 4.0 International License.

[Read Full License](#)

---

# Chiral Phonons in Biocrystals

Won Jin Choi<sup>1,2†</sup>, Keiichi Yano<sup>2,3†‡</sup>, Minjeong Cha<sup>1,2</sup>, Felipe M. Colombari<sup>4</sup>, Yichun Wang<sup>2,5,6</sup>, Sang Hyun Lee<sup>2,7</sup>, John M. Kruger<sup>8</sup>, André F. de Moura<sup>9\*</sup> and Nicholas A. Kotov<sup>1,2,3,5,10\*</sup>

<sup>1</sup>Department of Materials Science and Engineering, University of Michigan, Ann Arbor, MI 48109, USA;

<sup>2</sup>Biointerfaces Institute, University of Michigan, Ann Arbor, MI 48109, USA;

<sup>3</sup>Department of Chemical Engineering, University of Michigan, Ann Arbor, MI 48109, USA;

<sup>4</sup>Brazilian Biorenewables National Laboratory (LNBR), Brazilian Center for Research in Energy and Materials (CNPEM), Campinas, SP, 13.083-100, Brazil;

<sup>5</sup>Department of Biomedical Engineering, University of Michigan, Ann Arbor, MI 48109, USA;

<sup>6</sup>Department of Chemical and Biochemical Engineering, University of Notre Dame, South Bend, IN 46556, USA

<sup>7</sup>Department of Electrical Engineering and Computer Science, University of Michigan, Ann Arbor, MI 48109, USA;

<sup>8</sup>Department of Small Animal Clinical Sciences, Michigan State University, East Lansing, MI 48824, USA;

<sup>9</sup>Department of Chemistry, Federal University of São Carlos, São Carlos, SP, 13.565-905, Brazil;

<sup>10</sup>Program in Macromolecular Science and Engineering, University of Michigan, Ann Arbor, MI 48109, USA;

\*Correspondence to: [moura@ufscar.br](mailto:moura@ufscar.br) (A.F.M.), [kotov@umich.edu](mailto:kotov@umich.edu) (N.A.K.)

†Both authors contributed equally to this work.

‡Present address: Institute of Technology, Shimizu Corporation, Etchujima 3-4-17, Koto-ku, Tokyo 135-8530, Japan.

**ABSTRACT:** Chiral phonons are concerted mirror-symmetric movements of atomic groups connected by covalent and intermolecular bonds. Finding chiral phonons in biocrystals is fundamentally and technologically important because these lattice vibrations should be highly specific to their short- and long-range organizations. Based on theoretical and experimental data they might be expected but not identified or utilized. Here we show that terahertz chiroptical spectroscopy enables registration and attribution of chiral

**phonons in microcrystals of numerous amino acids and dipeptides. Theoretical analysis and computer simulations confirm that sharp mirror-symmetric bands observed for left and right enantiomers originate from collective vibrations of biomolecules interconnected by hydrogen bonds into helical chains. Structure-property relationships for strong phonons with rotatory components in biocrystals were also identified. Bladder stones and health supplements display strong spectral signatures of chiral phonons indicating their immediate importance for biomedicine.**

The vibrations in simple crystal lattices, typically described as longitudinal and transverse phonons, commonly consist of parallel or perpendicular oscillatory displacements of atoms, in respect to the propagation direction. As the complexity of the crystal lattice increases, the normal modes of phonons may become chiral as rotatory components emerge. Besides their fundamental significance, the chiral phonons favoring specific mirror-symmetrical left- and right-handed modes could be uniquely suitable for application in a range of emergent chiroptical technologies<sup>1-9</sup> but macroscale materials supporting such lattice vibrations have not been hitherto identified.

Chiral phonons were initially predicted computationally and then recognized spectroscopically in two-dimensional materials, such as MoS<sub>2</sub> and WSe<sub>2</sub><sup>1-4</sup>. The hexagonal lattices of these monolayer materials are, however, achiral. The left and right modes coexist as degenerate phononic states, which make their individual observation and utilization difficult because the chiroptical light polarization effects from these lattice vibrations cancel out each other in bulk materials. One can hypothesize that chiral phonons with specific polarization should be common for crystals from mirror-asymmetric biomolecules, which for brevity will

henceforth be referred to as *biocrystals*. Depending on the dispersion relations and the photon-phonon coupling strengths, the modes with left and right rotational components can be potentially detected by chiroptical spectroscopy because the degeneracy of the phonon states is lifted in biocrystals. The relationships between the asymmetry of the biomolecules forming the crystal lattice, their space group, and the normal modes of sustained phonons are some of the fundamental unanswered questions that could be addressed after that. Additionally, the different modes of chiral phonons in biocrystals would provide a unique tool for probing biomolecular arrangements in a wide range of structures with direct relevance to drug synthesis, biochemical quality control, protein folding, and disease diagnostics<sup>10-13</sup>.

Large number of studies were carried out in the past on terahertz (THz) and other parts of the electromagnetic spectrum on crystals of chiral biomolecules<sup>14-21</sup>. While some resonance peaks were observed<sup>17-21</sup>, the assignment of specific vibrations to these peaks was limited by quality and variety of spectroscopic data and computational tools needed are much more complex than those in MoS<sub>2</sub>, or WSe<sub>2</sub>. Furthermore, mirror symmetrical relations between potential left- and right- phonons were never observed. Several methodological problems have thus far prevented the observation of chiral phonons in biological crystals. Specific chemical structures of prospective biomolecules, preferred crystal lattices, and spectroscopic modalities for the observation of chiral phonons are not known. Even their expected spectral range is ambiguous, because the non-covalent interactions defining the structure and deformations in biocrystals can theoretically cover a wide range of vibrational frequencies<sup>13,22</sup>, leading to large spectral shifts compared to those of Weyl semimetals<sup>4,23</sup>. Furthermore, computational predictions of the collective vibrational modes of crystals with complex unit cells are also problematic. The diversity of non-covalent interactions, non-harmonicity and multiplicity of the coupled modes

possible for biocrystals necessitate large models and thus become computationally too expensive, especially for long-period oscillations involving the collective movement of multiple molecular segments<sup>20,24,25</sup> that are characteristic of phonons. Numerical errors arising from convergence tolerances further exacerbate computational challenges, especially for *in-silico* discovery of low frequency modes<sup>20,24</sup>.

Based on prior spectroscopic studies of proteins, DNA, and amino acids<sup>20,22,25-30</sup>, we hypothesized that chiral phonons in biocrystals would be located in the far-infrared (IR) to spectral window. While the resonance frequencies of ‘localized’ intermolecular vibrations of non-covalent interactions mostly lie in the mid-IR range, the phononic modes of biocrystals are likely to be observed between 0.2 and 3 THz (6 to 100  $\text{cm}^{-1}$ ) since the energies of their intermolecular forces lie between  $\sim 0.001$  and  $\sim 0.02$  eV, matching the photon energies of THz radiation. The molecular masses of units undergoing these vibrational motions are also relatively large ( $>50$  g/mol)<sup>22,25,28</sup>, which dramatically reduces the phonon frequencies compared to inorganic crystals.

We chose amino acids (AAs) as experimental and computational models because they are structurally versatile and serve as building blocks for many biomolecules. They are also known to have absorption bands of uncertain origin in the far-IR and THz ranges<sup>20,25,29,30</sup>. Importantly, almost all AAs are available as left/right enantiomers and computational difficulties related to calculations of chiral phonons can be addressed accurately and efficiently with the recently developed semiempirical GFN2-XTB Hamiltonian<sup>31</sup>.

However, AAs also have disadvantages as experimental models for chiral phonons, due to the coexistence of multiple crystalline phases and hydration states in their bulk crystals. The seemingly minor presence of the opposite enantiomer and impurities can also distort or change

their crystal habits<sup>11,22</sup>. Furthermore, AA powders and pellets have a wide range of particle sizes with crystals larger than 200  $\mu\text{m}$  persisting even after grinding. Large dimensions and multiple crystal habits severely deteriorate the quality of THz absorption (TA)<sup>32</sup> and THz circular dichroism (TCD) spectra due to Mie scattering (**Supplementary Information**), resulting in broadened spectra with distorted peak features. A further challenge in this study is that the implementation of chiroptical spectroscopy methods in the THz range is far from being trivial especially for biological materials<sup>33–35</sup>.

To obtain high quality spectra of the biocrystals, we developed a hyperspectral THz setup with motorized XY scanning (**Fig. 1**). This setup enables accurate measurements and identification of chiral phonons by acquiring spatially resolved TA, TCD, and THz optical rotation dispersion (TORD) spectra (**Fig. 1**) in concentrated slurries containing ~ 50 wt% of recrystallized AA crystals in mineral oil (MO). The random orientation of the densely packed microcrystals in the slurries eliminates spectral distortions typically observed in pressured and pelleted samples arising from birefringence and linear dichroism (**Fig. 1a,b** and **Supplementary Information**). Similar problems were reported for circular dichroism measurements in the visible range<sup>36,37</sup>.

A quartz sandwich cell with a 100  $\mu\text{m}$  spacer maintaining the uniformity of the optical wavefront and sample thickness was utilized to obtain high signal-to-noise ratios. Also important was maintaining crystal phase purity and AA crystal sizes below 20  $\mu\text{m}$ , which was achieved by careful recrystallization of the commercial chemicals (**Supplementary Fig. 1** and **Supplementary Tables 1, 2**). Their crystalline phase and size distributions were confirmed by powder X-ray diffraction (XRD) analysis, scanning electron microscopy (SEM) and particle size analyzers, respectively (**Fig. 1c,d** and **Supplementary Figs. 2-5**).

The TA for each pixel is calculated directly from  $E_x$  and  $E_y$ , fast Fourier transform of the electric fields in the  $x$  and  $y$  directions obtained by three different polarization measurements, while TCD and TORD spectra for each pixel were determined from the Stokes equations (**Fig. 1f-g** and **Supplementary Information**)<sup>33,34</sup>. The TA spectra for the  $L$  and  $D$  enantiomers of the 20 AAs obtained in this study (**Fig. 2a,b**) as well as the TA spectra observed for their subset using pelleted samples in prior studies<sup>20,25,29</sup> consistently indicate that the molecular structure alone cannot explain their THz spectral features. For example, the one-carbon-atom difference in the side chains of aspartic acid, Asp, and glutamic acid, Glu, leads to a drastic change in the number, position, and width of all the TA peaks (**Fig. 2a,b** and **Supplementary Fig. 12**). The same conclusion can also be reached by analyzing the TA spectra using a dynamic time-warping (DTW) algorithm and ‘violin’ plots. Both of these methods reveal inconsistencies of TA spectra grouping according to the hydrophobic, charged or uncharged side chains in AA (**Fig. 2c,d**), which means that local vibrational modes (i.e. *within* molecular segments) are unable to explain THz oscillatory phenomena. This conclusion is further substantiated by quantum mechanical (QM) calculations of the THz spectra of individual AA molecules, which differ strongly from the experimentally observed spectra (**Supplementary Figs. 17-20** and a **Supplementary Video 1** file titled *Single Molecule Vibrations*).

Two dominant types of TA spectra can be recognized for all AAs in **Fig. 2d-f**. *Type 1* spectra, exemplified by methionine (Met), show monotonically increasing absorptions with broad peaks, whereas *Type 2* spectra, exemplified by glutamine (Gln) or glutamic acid (Glu), display multiple sharp peaks. Note that attribution to *Type 1* or *Type 2* does not correlate with the chemical properties of the side chains (i.e. mass, charge and hydrophobicity), whereas a distinct negative correlation between the molecular masses of the AAs and the lowest THz

resonance peak positions for both types of TA spectra (**Fig. 2g**) was observed. Such dependence on molecular mass indicates that the collective long-range displacements of AA molecules or their large segments are responsible for these peaks<sup>38</sup>.

Going further, we found that *Type 1* and *Type 2* spectra are nearly perfectly correlated with the symmetry group of the unit cell of the AA crystals (table S2). All five *Type 2* AAs crystallize in the orthorhombic space group  $P2_12_12_1$  - the most common for biocrystals<sup>39</sup> (**Fig. 2f**). *Type 1* AAs crystallize in monoclinic space groups  $P2_1$  or  $C2$  (**Fig. 2e**). By comparing the XRD data with THz spectra, one can see that the crystallinity is the key requirement for the observation of the sharp TA peaks: subtle changes in XRD result in distinctly different features in the TA spectra (**Supplementary Figs. 6,7**). Concomitantly, the absence of the long-range order leads to featureless, broad spectra (**Supplementary Fig. 8**)<sup>22,40</sup>. It therefore becomes clear that the sharp peaks at the low frequency observed for *Type 2* AAs are associated with well-resolved phonon modes. The broad peaks in crystals of *Type 1* and *Type 2* AAs are expected to be a superposition of multiple phonons and other vibrational modes.

The sharp peaks in the spectra of *Type 2* AAs were investigated in greater detail. The  $P2_12_12_1$  space group, uniting this type of biocrystals, has three  $2_1$  screw axes producing chiral patterns inside the unit cell. Correspondingly, the nitrogen atoms of the amine groups ( $-NH_2$ ) and  $N-H\cdots O$  hydrogen bonds form helices in the unit cell (e.g., *L*-Glu in **Fig. 3c**). To investigate the mirror asymmetry of the observed phononic modes, TCD and TORD spectra of AAs and their enantiomers were obtained (**Fig. 3a,b** and **Supplementary Fig 12**). All five *Type 2* AAs (His, Glu, Gln, Thr, Tyr) forming crystals in the  $P2_12_12_1$  space group showed distinct bisignate TCD peaks at low frequency, with nearly perfect mirror symmetry for *L* and *D* enantiomers, clearly indicating the chirality of these phonons (**Fig. 3a,b,h,i** and **Supplementary**

**Fig 14).** Other AAs may also support some modes of chiral phonons but their TCD spectra are broad, these features being likely to form from the superposition of multiple overlapping modes (**Supplementary Fig. 12**).

Born-Kuhn (BK) model of coupled bi-oscillators<sup>41,42</sup> may provide heuristic level of understanding of chiral phonons in various biocrystals. Unlike previous versions of BK used for chiral plasmons<sup>41,42</sup>, the bi-oscillators in **Fig. 3d,e** represent AA segments coupled via hydrogen bonds. They are stacked on top of each other with twists between the molecules, similar to the P2<sub>1</sub>2<sub>1</sub>2<sub>1</sub> lattice in **Fig. 3c**. A left- or right-circularly polarized beam matching the handedness of the bi-oscillators can thereby excite their collective vibrations (**Fig. 3d,e**). The polarization-dependent light absorption is represented by the nonlocality tensor  $\mathbf{\Gamma}(k, \omega)$ , and for the model in **Fig. 3c** it acquires the form:

$$\mathbf{\Gamma}(k, \omega) = \frac{DN_0e^2}{3m} \frac{\xi}{(\omega_0^2 - i\gamma\omega - \omega^2)^2 - \xi^2}, \quad \text{Eq. 1}$$

where,  $\omega_0$  is the resonance frequency,  $\gamma$  is damping parameter,  $\xi$  is the coupling strength between the two oscillators, and  $m$  is mass of the individual oscillator; the remaining constants and variables are given in Supplementary Information. The inverse dependence of  $\mathbf{\Gamma}(k, \omega)$  on  $m$  in Eq. 1 rationalizes the empirically observed inverse relationship between the TA peak position and molecular mass of AA (**Fig. 2g**). TCD and TORD spectra can be calculated from  $\mathbf{\Gamma}(k, \omega)$  by applying the Drude–Born–Fedorov formalism<sup>41,42</sup> as

$$TCD = \frac{2\omega}{c} \text{Im}\{\mathbf{\Gamma}\} \quad \text{Eq. 2}$$

$$TORD = \frac{\omega}{2c} \text{Re}\{\mathbf{\Gamma}\}, \quad \text{Eq. 3}$$

where  $c$  and  $\omega$  are the speed of light and oscillation frequency, respectively (**Supplementary Information**). The calculated TCD and TORD spectra match the shape and position of the experimental ones very well (**Fig. 3h,i** and **Supplementary Fig. 14**). As perhaps expected, increases in the coupling parameter  $\xi$  increase the amplitude of the TCD and TORD peaks, which shows that stronger intermolecular bonds in biocrystals promote the propagation of chiral phonons (**Fig. 3g**). Concurrently, increase in the damping parameter  $\gamma$  reduces the intensity of the chiroptical THz peaks (**Fig. 3f**). Since both  $\xi$  and  $\gamma$  strongly influence the shapes of the TCD and, in particular, TORD peak, one can confidently fit the experimental data with the BK model obtaining the values of  $\gamma$  and  $\xi$  (**Supplementary Table 5**) for several *Type 2* AAs (**Fig. 3h,i** and **Supplementary Fig. 14**). We found that the damping parameter<sup>43,44</sup> decreases with the increase of the polarizability,  $\mu$ , of the AA constituting the crystals (**Fig. 3j**), which can facilitate the selection of biocrystals predisposed to high-intensity chiral phonons.

Further insight into the nature of lattice vibrations in crystals of AAs was obtained from atomistic computer simulations. A periodic supercell containing  $2 \times 1 \times 2$  unit cells of *L*-Glu was used for calculations of the phonon normal modes at the QM level using the GFN2-XTB Hamiltonian<sup>31</sup> (**Fig. 3k**), as implemented in the CP2K program<sup>45</sup> (**Supplementary Information**). The calculated TA (**Fig. 3l**) and TCD (**Fig. 3m**) spectra agree with the experimental results (**Fig. 2f** and **Fig. 3h**). The computer simulations also enable identification of the actual chiral phonon modes responsible for the appearance of the peaks in the TCD spectra. As such, the normal mode for the 1.2-1.4 THz peak in crystals of *L*-Glu involves twisting of the carboxylate groups from both the main chain and the side chain with dihedral angles changing by tens of degrees (**Fig. 3n**, **Supplementary Information** and a **Supplementary Video2** file titled *Chiral Phonons*). The handedness of the rotatory motion of these groups is opposite for the two Glu

enantiomers (**Fig. 3h,m**). The broad peaks observed for *Type 1* AAs represent superposition of several normal modes, as exemplified for the lattice vibrations observed for *L*-Met (**Supplementary Fig. 18**, a **Supplementary Video 2** file titled *Chiral Phonons*). Comparison of the crystallographically-derived structures of the AAs shows the structural differences between the two types of AA crystals. In *Type 1* AAs the side chains interact mostly by via van der Waals forces while the main chains are strongly bound by ionic interactions between charged groups. On the other hand, charged or polar groups in the side chains of *Type 2* AAs, allow for the formation of a homogeneous and strong network of supramolecular bonds throughout the crystal, which leads to the emergence of sharp TA, TCD, TORD peaks as spectroscopic signatures of chiral phonons and concurs with the high values of coupling parameter  $\xi$  established using the BK model. Besides its importance in rationalizing the TA and TCD results for various biocrystals, this structure-function relationship opens the possibility to ‘tune’ chiral phonon frequencies in engineered synthetic crystals.

The concerted movement of many atoms characteristic for chiral phonons (**Supplementary Video 2**) makes them highly sensitive to the both short- and long-range organization of the molecular lattices. In the context of this study, this is essential because this sensitivity of chiral phonons makes possible their utilization in biomedical technologies. To demonstrate this capability and illustrate the generality of chiral phonons in biocrystals, TA, TCD, and TORD spectra of dipeptides, including Ala-Ala, Ala-Tyr, Ala-Gln, Gly-Gly as well as cystine (Cys-Cys linked via S-S bonds, CYT), and carnosine (Ala-His, CAR) were acquired (**Fig. 4** and **Supplementary Fig. 16**). Among these six dipeptides, Ala-Ala, Gln-Gln, Cys-Cys, and Ala-His display the strongest signatures of chiral phonons. Note that *L*-CYT is the key component of kidney and bladder stones<sup>46</sup>, hair, nails, and skin, while *L*-CAR is known to

scavenge reactive oxygen species<sup>47</sup> and formulations of its microcrystals are used as nutritional supplements, which prompted us to investigate them in greater details.

*L*-CYT crystallizes as hexagonal plates (P6<sub>1</sub>22 chiral space group,  $a = b = 0.54$  nm,  $c = 5.60$  nm) and the six CYT molecules in the unit cell are helically organized about the 6<sub>1</sub> screw axis (**Fig. 4a**)<sup>46</sup>. Similar to *Type 2* AAs, TA spectra of *L*- and *D*-CYT show sharp peaks in the spectral window between 0.2 and 2.5 THz (**Fig. 4b**). The lowest resonance peak positions at 0.71 THz and 0.56 THz shown in **Fig. 2g** agree well with the molecular weight of CYT (240.3 g/mol) and CAR (226.23 g/mol), respectively. TCD spectra of CYT enantiomers display mirror-symmetrical peaks (**Fig. 4b**) with the most intense TCD peak at 1.57 THz matching very well with the TCD predictions from simulations of the CYT supercell (**Supplementary Fig. 19** and **Supplementary Movies**). The attribution of both bands to chiral phonons was also confirmed by the spectroscopic data for *DL*-CYT and deuterated *L*-CYT (**Supplementary Fig. 15**). Similarly, the TA and TCD spectra of *L*-CAR show collective vibrational modes having distinct TCD peaks (**Fig. 4b**). Alanine-based dipeptides (Ala-Ala, Ala-Tyr, and Ala-Gln) other than *L*-CAR were also measured and the results are depicted in figs. S16 and **Fig. 2g**.

The sharpness of the TCD peaks, the selective identification of left and right modes of chiral phonons corresponding to the enantiomers of the biomolecules, and the sensitivity of their spectral attributes to small perturbations, suggest the utility of the spectroscopic toolbox for chiral phonons in biocrystals in a variety of potential biomedical and pharmaceutical applications. The non-destructive and non-ionizing nature of THz spectroscopy presents an additional benefit in this context<sup>10,11,35,48</sup>, which is essential both for the patients and doctors. To evaluate the feasibility of such applications, we analyzed four naturally occurring cystine stones removed from two canine patients as part of standard veterinary medical care (**Fig. 4c**). These stones

showed strong TA peaks at exactly 0.71 THz, where the CYT slurry showed its strongest resonance (**Fig. 4b,d**). Hyperspectral THz mapping shows not only the size and position of the stones but also provides a phononic fingerprint of the chemical composition that cannot be obtained using X-ray diffraction (**Fig. 4e,f**). A negative-to-positive transition in the TCD was found in the central part of the stones and birefringence effects in the edges and non-flat areas indicate variations in the growth conditions and crystallization patterns of the stones within the patients. This method could potentially be adapted to diagnosis and analysis of calculi in the urinary bladder or kidneys.

The variability of chiral phonon signatures from *L*-CAR was also tested in commercial health supplements from five different manufacturers (**Fig. 4g**). TA and TCD spectra (**Fig. 4h,i**) show large differences between the *L*-CAR formulations (**Fig. 4b**). Ideally, the intensities of TA and TCD peaks should have the same ratio in all of the products and minimal sample-to-sample variations. However, this was not the case, as can be visualized by the TA and TCD distribution maps. These maps show distinct peak correlations specific to each manufacturer (**Fig. 4j,l**), which can be associated with structural differences in the *L*-CAR biocrystals and impurities. Since intermolecular interactions in biocrystals are also sensitive to aging caused by different environmental factors<sup>49</sup>, the changes in TA and TCD spectra of *L*-CAR samples after heating at 65 °C for 48 hours were also evaluated. The data in **Fig. 4k,m** indicate that: (1) the phonon of the *L*-CAR biocrystals is temperature-sensitive, even when the environment is far below its melting temperature ( $T_{melt} = 253$  °C) and (2) changes occurring in TA and TCD spectra with temperature are specific to each manufacturer presumably due to various chiral and achiral additives. The observed tightening of the TCD spectra around the central point after thermal

aging indicate that both recrystallization processes and chemical reactions have taken place even though appearance of the supplement does not change.

In conclusion, the identification of chiral phonons in the THz range in biocrystals, and the elaboration of a spectroscopic toolbox for them, opens the door to a large family of materials wherein the complex collective vibrations of crystal lattices with rotatory components can be investigated. Due to the strong sensitivity of chiral phonons to the chemical interactions in the crystal lattice, this methodological toolbox can be used for quality control in biomedical industry<sup>10,11</sup>, biomedical imaging<sup>8,48</sup>, and chiral photonics<sup>50</sup>. The library of THz fingerprints from basic AAs to complex proteins and other biomolecular complexes would open a new horizon for THz bioinformatics and deepen our understanding of many collective-vibration-mediated (bio)chemical processes.

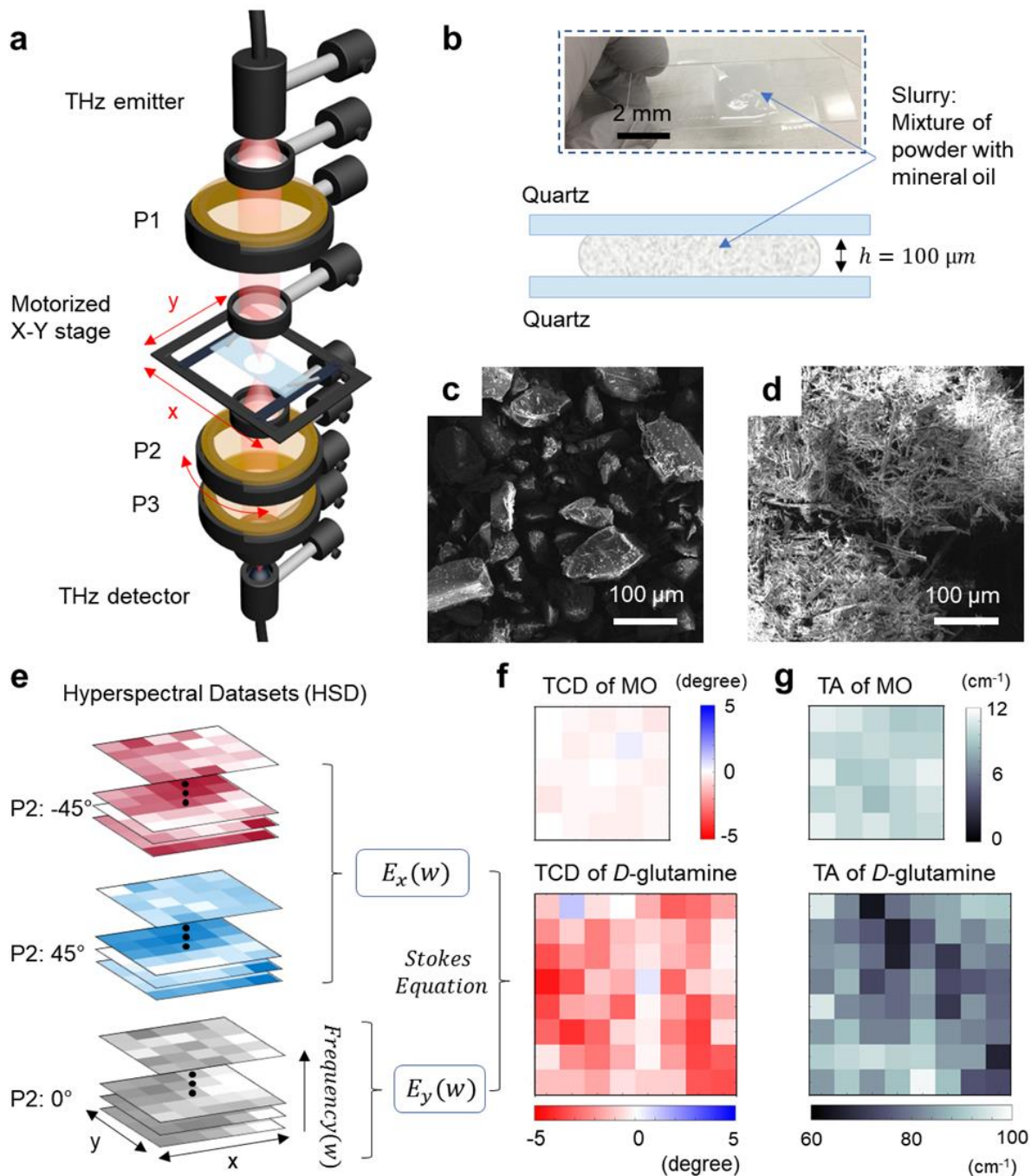


**Fig. 1 Hyperspectral THz-TDP set-up for observation of chiral phonons in AA microcrystals.** **a**, Schematics of the THz-TDP setup. Three wire grid polarizers (P1, P2 and P3) were used to analyze polarization states of the beam after passing through the sample. A motorized X-Y stage was used for mapping. **b**, Photograph and schematic of sandwich quartz cell with slurry mixtures, respectively. **c** and **d**, SEM images of before (**c**) and after (**d**) recrystallization of *L*-glutamine. **e**, Fourier-transformed hyperspectral datasets of electric fields

were measured by three different polarization measurements for each pixel.  $E_x(\omega)$  is obtained from the measurements of  $45^\circ$  and  $-45^\circ$  for the P2 polarizer and  $E_y(\omega)$  is from  $0^\circ$ , which is along the  $y$  direction. **f**, Example of TCD mapping for reference mineral oil and *D*-glutamine at 1.69 THz, respectively. **g**, Example of TA mapping for reference mineral oil and *D*-glutamine at 1.69 THz, respectively. The size of each pixel in the images of (**e-g**) is  $500 \mu\text{m}$ .

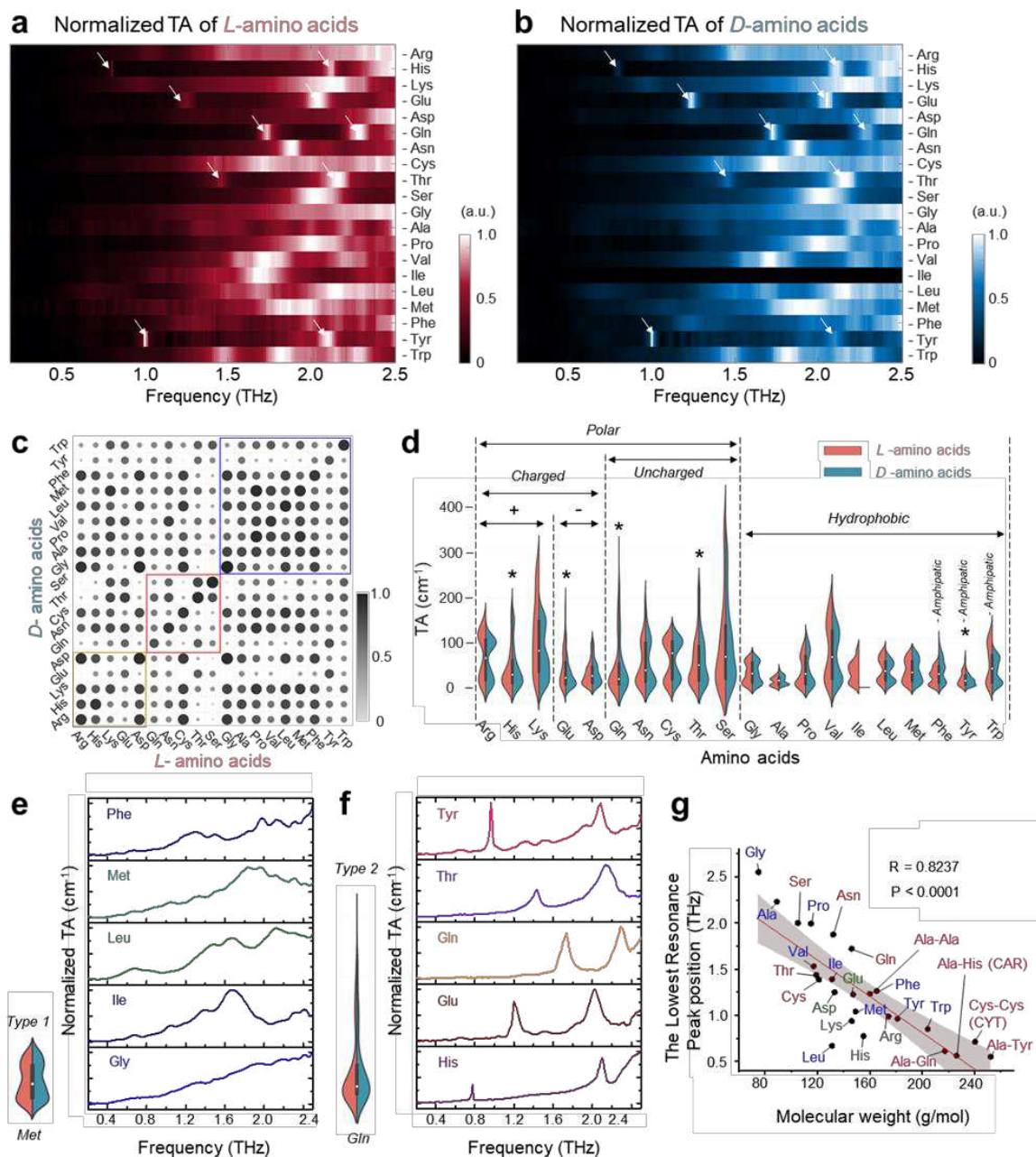


**Fig. 2 Analysis of TA spectra for *L* and *D* enantiomers of 20 AAs.** **a** and **b**, 2D plot of TA spectra with band intensity represented by the color brightness. The same samples of achiral glycine were used for the TA analysis. White arrows indicate the appearance of sharp peaks in the spectra. **c**, 2D correlation matrix between *L*- and *D*-AAs without isoleucine. Larger sizes and darker colors indicate higher degrees of similarity between AAs. Some groups show similarity as indicated by square boxes; blue for hydrophobic, red for uncharged polar and gold for charged polar side groups. **d**, ‘Split violin’ side-by-side plots for TA spectra of the two enantiomers of AAs. The left half shows those of *L*-AAs and the right shows those of *D*-AAs. **e** and **f**,

Normalized TA spectra of five representative *L*-AAs having broad peaks and sharp peaks, respectively. The shape of the distribution is dependent on the width of the peaks: broad peak AAs – *Type 1*, sharp peak AAs – *Type 2*. **g**, Molecular weight dependence of the lowest THz resonance peak position. The lowest peak appearing above the baseline was chosen for each AA crystal and the exact peak positions of the absorption peaks are summarized in Table S4. Color labels correspond to different groups; gray - positively charged polar, green - negatively charged polar, red - uncharged polar, blue - hydrophobic AAs and pink - dipeptides. AAs with larger molecular mass show lower resonance frequencies.

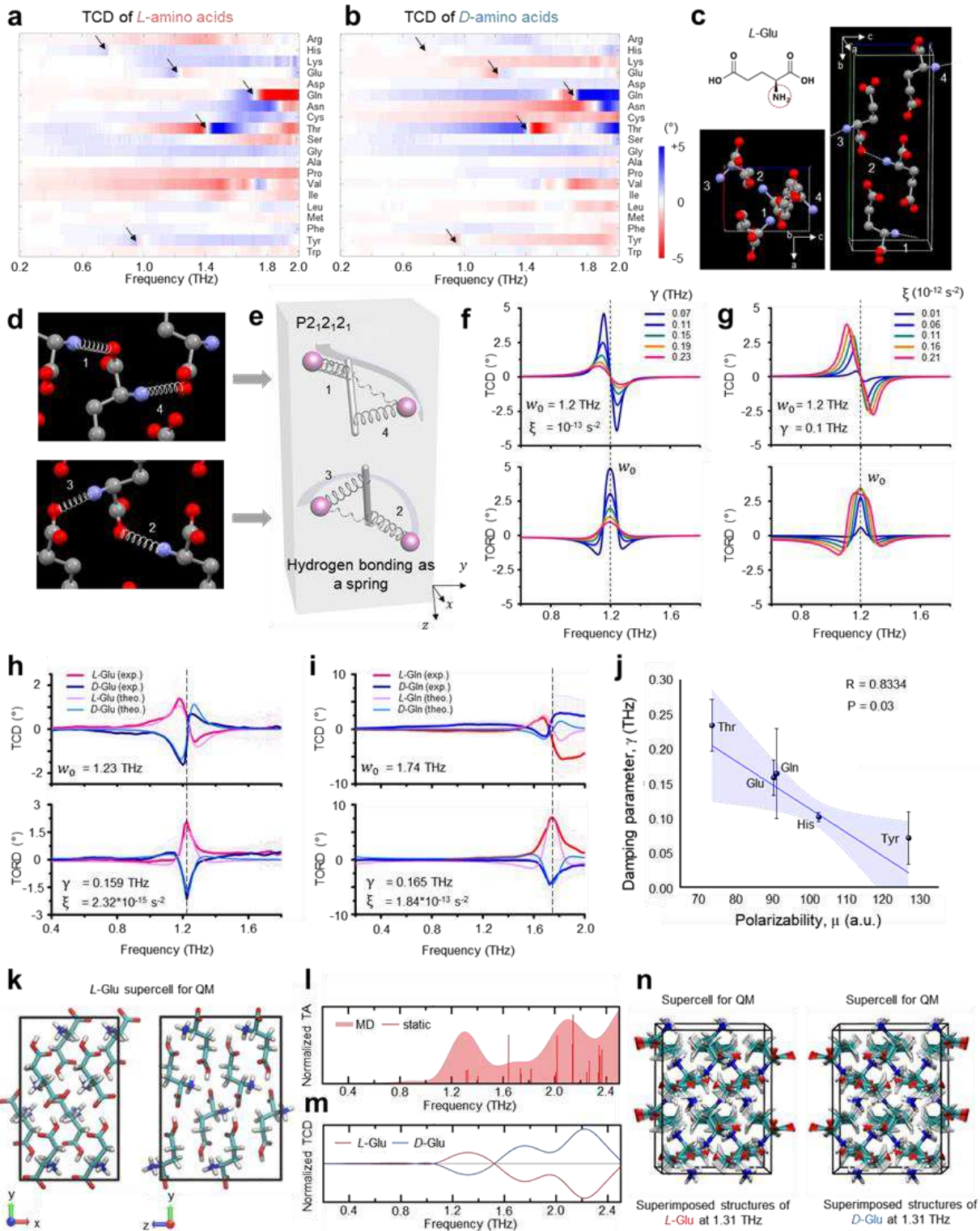


**Fig. 3 Analysis of TCD and TORD spectra for *L*- and *D*-enantiomers of 20 AAs. **a** and **b**, 2D plot of TCD from 20 proteinogenic *L*- and *D*-AAs, respectively. *D*-isoleucine was not available. The same sample of glycine was used for analysis of both *L*- and *D*-AAs. Black arrows indicate crossing zero points corresponding to resonance frequency,  $\omega_0$  from Eq. 1. **c**, Molecular configuration of *L*-Glu crystal cell as an example of a compound crystallizing in the  $P2_12_12_1$  space group. Amine groups are helically arranged in the 1-2-3-4 progression. **d**, Enlarged view of hydrogen bonds in (c), represented as springs in the BK model used for heuristic description of chiral phonons. **e**, Schematic representation of the unit cell with bi-oscillators in  $P2_12_12_1$  space symmetry. **f** and **g**, TCD and TORD calculated from the BK model varying with damping parameter  $\gamma$  and coupling strength  $\xi$ . **h** and **i**, Experimental and calculated TCD and TORD spectra of Glu and Gln, respectively. **j**, Dependence of  $\gamma$  on the polarizability ( $\mu$ ) of AA molecules<sup>43,44</sup>. **k**, Supercell of *L*-Glu used for the QM computations of THz spectra. **l**, Normalized TA spectra obtained from calculations of the *L*-Glu supercell in (k) using normal mode analysis (vertical lines) and MD simulations at the QM level (solid surfaces). **m**, Normalized TCD spectra from the same MD simulations at the QM level used for TA in (l). **n**, Superimposed structures of the *L*-Glu molecules along the normal mode (eigenmode) with a frequency of 1.31 THz for the system depicted in (k) (left) and its mirror image (right).**

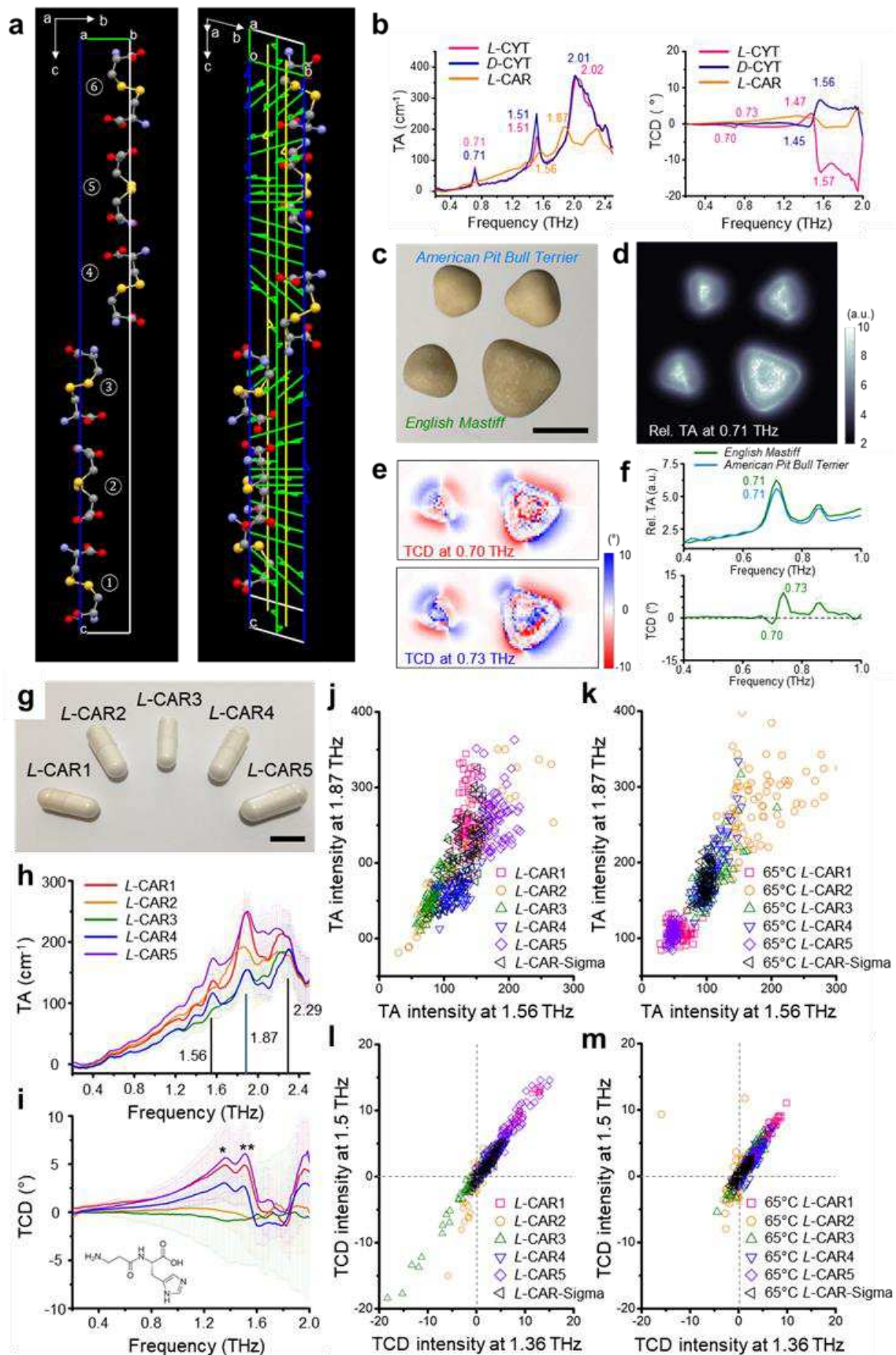


**Fig. 4 Chiral phonons in CYS and CAR.** **a**, Helical axis of *L*-CYT molecules in a unit cell. Six *L*-CYT molecules winding a  $6_1$  screw axis that coincides with the *c*-axis as indicated by green helical 'scaffold'. **b**, Averaged TA and TCD spectra from *L*-CYT, *D*-CYT and *L*-CAR. **c**, Photograph of four cystine stones from two canine patients. The upper two stones are from a seven-year-old male *American pit bull terrier* and the lower two stones are from a six-year-old male *English mastiff*, respectively. Scale bar is 5 mm. **d**, Relative TA map of four cystine stones at 0.71 THz. **e**, TCD map of cystine stones from *English mastiff* at 0.7 THz and 0.73 THz, respectively. A negative-to-positive transition in the TCD was found in the central part of the stones, while there are birefringence effects in the edges and non-flat areas, indicating variations in the growth conditions and crystallization patterns of the stones. **f**, Averaged TA and TCD spectra from cystine stones matched well with that of *L*-CYT crystals prepared *in vitro*. **g**, Photograph of five different pills from various manufacturers used for measurements. Scale bar is 1 cm. **h** and **i**, Average TA and TCD spectra from as-received *L*-CAR from five different manufacturers. **j** and **l**, 2D peak intensity distribution map of TA and TCD from as-received *L*-CAR samples. **k** and **m**, 2D peak intensity distribution map of TA and TCD from *L*-CAR slurries after incubation at 65 °C for 48 h.

## REFERENCES

1. Zhu, H. *et al.* Observation of chiral phonons. *Science* **359**, 579–582 (2018).
2. Chen, X. *et al.* Entanglement of single-photons and chiral phonons in atomically thin WSe<sub>2</sub>. *Nat. Phys.* **15**, 221–227 (2019).
3. Zhang, L. & Niu, Q. Chiral Phonons at High-Symmetry Points in Monolayer Hexagonal Lattices. *Phys. Rev. Lett.* **115**, 1–5 (2015).
4. Yuan, X. *et al.* The discovery of dynamic chiral anomaly in a Weyl semimetal NbAs. *Nat. Commun.* **11**, 1–7 (2020).
5. Yeom, J. *et al.* Chiro-magnetic nanoparticles and gels. *Science* **359**, 309–314 (2018).
6. Valev, V. K., Baumberg, J. J., Sibilica, C. & Verbiest, T. Chirality and chiroptical effects in plasmonic nanostructures: Fundamentals, recent progress, and outlook. *Adv. Mater.* **25**, 2517–2534 (2013).
7. Hooper, D. C. *et al.* Strong Rotational Anisotropies Affect Nonlinear Chiral Metamaterials. *Adv. Mater.* **29**, (2017).
8. Oh, S. J. *et al.* Nanoparticle-enabled terahertz imaging for cancer diagnosis. *Opt. Express* **17**, 3469 (2009).
9. Ma, W. *et al.* Chiral Inorganic Nanostructures. *Chem. Rev.* **117**, 8041–8093 (2017).
10. Shen, Y. C. Terahertz pulsed spectroscopy and imaging for pharmaceutical applications: A review. *Int. J. Pharm.* **417**, 48–60 (2011).
11. Zeitler, J. A. *et al.* Terahertz pulsed spectroscopy and imaging in the pharmaceutical setting - a review. *J. Pharm. Pharmacol.* **59**, 209–223 (2007).
12. Keiderling, T. A. Protein and peptide secondary structure and conformational determination with vibrational circular dichroism. *Curr. Opin. Chem. Biol.* **6**, 682–688 (2002).
13. Woutersen, S. *et al.* Peptide conformational heterogeneity revealed from nonlinear vibrational spectroscopy and molecular-dynamics simulations. *J. Chem. Phys.* **117**, 6833–6840 (2002).
14. Zhang, Y., De Juan, F., Grushin, A. G., Felser, C. & Sun, Y. Strong bulk photovoltaic effect in chiral crystals in the visible spectrum. *Phys. Rev. B* **10**, 245206 (2019).
15. Jähnigen, S., Scherrer, A., Vuilleumier, R. & Sebastiani, D. Chiral Crystal Packing Induces Enhancement of Vibrational Circular Dichroism. *Angew. Chemie - Int. Ed.* **57**, 13344–13348 (2018).
16. Kanda, N., Konishi, K., Nemoto, N., Midorikawa, K. & Kuwata-Gonokami, M. Real-time broadband terahertz spectroscopic imaging by using a high-sensitivity terahertz camera. *Sci. Rep.* **7**, 1–10 (2017).
17. Williams, M. R. C. *et al.* Terahertz spectroscopy of enantiopure and racemic polycrystalline valine. *Phys. Chem. Chem. Phys.* **13**, 11719–11730 (2011).
18. King, M. D., Buchanan, W. D. & Korter, T. M. Investigating the anharmonicity of lattice vibrations in water-containing molecular crystals through the terahertz spectroscopy of l-serine monohydrate. *J. Phys. Chem. A* **114**, 9570–9578 (2010).
19. Korter, T. M. & Plusquellic, D. F. Continuous-wave terahertz spectroscopy of biotin: Vibrational anharmonicity in the far-infrared. *Chem. Phys. Lett.* **385**, 45–51 (2004).
20. Korter, T. M. *et al.* Terahertz spectroscopy of solid serine and cysteine. *Chem. Phys. Lett.* **418**, 65–70 (2006).
21. Plusquellic, D. F., Siegrist, K., Heilweil, E. J. & Esenturk, O. Applications of terahertz

- spectroscopy in biosystems. *ChemPhysChem* **8**, 2412–2431 (2007).
22. Walther, M., Fischer, B. M. & Jepsen, P. U. Noncovalent intermolecular forces in polycrystalline and amorphous saccharides in the far infrared. *Chem. Phys.* **288**, 261–268 (2003).
  23. Gao, Y. *et al.* Chiral terahertz wave emission from the Weyl semimetal TaAs. *Nat. Commun.* **11**, (2020).
  24. Jepsen, P. U. & Clark, S. J. Precise ab-initio prediction of terahertz vibrational modes in crystalline systems. *Chem. Phys. Lett.* **442**, 275–280 (2007).
  25. Williams, M. R. C., Aschaffenburg, D. J., Ofori-Okai, B. K. & Schmuttenmaer, C. A. Intermolecular vibrations in hydrophobic amino acid crystals: Experiments and calculations. *J. Phys. Chem. B* **117**, 10444–10461 (2013).
  26. Markelz, A. G., Roitberg, A. & Heilweil, E. J. Pulsed terahertz spectroscopy of DNA, bovine serum albumin and collagen between 0.1 and 2.0 THz. *Chem. Phys. Lett.* **320**, 42–48 (2000).
  27. Markelz, A., Whitmire, S., Hillebrecht, J. & Birge, R. THz time domain spectroscopy of biomolecular conformational modes. *Phys. Med. Biol.* **47**, 3797–3805 (2002).
  28. González-Jiménez, M. *et al.* Observation of coherent delocalized phonon-like modes in DNA under physiological conditions. *Nat. Commun.* **7**, (2016).
  29. Rungsawang, R., Ueno, Y., Tomita, I. & Ajito, K. Angle-dependent terahertz time-domain spectroscopy of amino acid single crystals. *J. Phys. Chem. B* **110**, 21259–21263 (2006).
  30. Singh, R., George, D. K., Benedict, J. B., Korter, T. M. & Markelz, A. G. Improved mode assignment for molecular crystals through anisotropic terahertz spectroscopy. *J. Phys. Chem. A* **116**, 10359–10364 (2012).
  31. Grimme, S., Bannwarth, C. & Shushkov, P. A Robust and Accurate Tight-Binding Quantum Chemical Method for Structures, Vibrational Frequencies, and Noncovalent Interactions of Large Molecular Systems Parametrized for All spd-Block Elements (Z = 1–86). *J. Chem. Theory Comput.* **13**, 1989–2009 (2017).
  32. Garet, F., Hofman, M., Meilhan, J., Simoens, F. & Coutaz, J. L. Evidence of Mie scattering at terahertz frequencies in powder materials. *Appl. Phys. Lett.* **105**, (2014).
  33. Choi, W. J. *et al.* Terahertz circular dichroism spectroscopy of biomaterials enabled by kirigami polarization modulators. *Nat. Mater.* **18**, 820–826 (2019).
  34. Kan, T. *et al.* Enantiomeric switching of chiral metamaterial for terahertz polarization modulation employing vertically deformable MEMS spirals. *Nat. Commun.* **6**, 1–7 (2015).
  35. Dhillon, S. S. *et al.* The 2017 terahertz science and technology roadmap. *Journal of Physics D: Applied Physics* **50**, 043001 (2017).
  36. Provenzano, C., Pagliusi, P., Mazzulla, A. & Cipparrone, G. Method for artifact-free circular dichroism measurements based on polarization grating. *Opt. Lett.* **35**, 1822 (2010).
  37. Claborn, K., Puklin-Faucher, E., Kurimoto, M., Kaminsky, W. & Kahr, B. Circular Dichroism Imaging Microscopy: Application to Enantiomorphous Twinning in Biaxial Crystals of 1,8-Dihydroxyanthraquinone. *J. Am. Chem. Soc.* **125**, 14825–14831 (2003).
  38. Burnett, A. D. *et al.* Effect of molecular size and particle shape on the terahertz absorption of a homologous series of tetraalkylammonium salts. *Anal. Chem.* **85**, 7926–7934 (2013).
  39. Wukovitz, S. W. & Yeates, T. Space-Groups Over Others. *Nat. Struct. Biol.* **2**, 1062–1067 (1995).
  40. Zhang, F. *et al.* Application of THz Vibrational Spectroscopy to Molecular Characterization and the Theoretical Fundamentals: An Illustration Using Saccharide

- Molecules. *Chem. - An Asian J.* **12**, 324–331 (2017).
41. Yin, X., Schäferling, M., Metzger, B. & Giessen, H. Interpreting chiral nanophotonic spectra: The plasmonic Born-Kuhn model. *Nano Lett.* **13**, 6238–6243 (2013).
  42. Davis, M. S., Zhu, W., Lee, J. K., Lezec, H. J. & Agrawal, A. Microscopic origin of the chiroptical response of optical media. *Sci. Adv.* **5**, (2019).
  43. Sala, J., Gurdia, E. & Masia, M. The polarizable point dipoles method with electrostatic damping: Implementation on a model system. *J. Chem. Phys.* **133**, (2010).
  44. Dos Santos, L. H. R., Krawczuk, A. & Macchi, P. Distributed atomic polarizabilities of amino acids and their hydrogen-bonded aggregates. *J. Phys. Chem. A* **119**, 3285–3298 (2015).
  45. Kühne, T. D. *et al.* CP2K: An electronic structure and molecular dynamics software package -Quickstep: Efficient and accurate electronic structure calculations. *J. Chem. Phys.* **152**, (2020).
  46. Rimer, J. D. *et al.* Crystal Growth Inhibitors for the Stones Through Molecular Design. *Science* **330**, 337–341 (2010).
  47. Neu, J. & Schmuttenmaer, C. A. Terahertz Spectroscopy and Density Functional Theory Investigation of the Dipeptide L-Carnosine. *J. Infrared, Millimeter, Terahertz Waves* **41**, 1366–1377 (2020).
  48. Fitzgerald, A. J. *et al.* An introduction to medical imaging with coherent terahertz frequency radiation. *Phys. Med. Biol.* **47**, (2002).
  49. Kawase, M. *et al.* Application of Terahertz absorption spectroscopy to evaluation of aging variation of medicine. *Anal. Sci.* **27**, 209–212 (2011).
  50. Xiong, R. *et al.* Biopolymeric photonic structures: Design, fabrication, and emerging applications. *Chem. Soc. Rev.* **49**, 983–1031 (2020).

# Figures

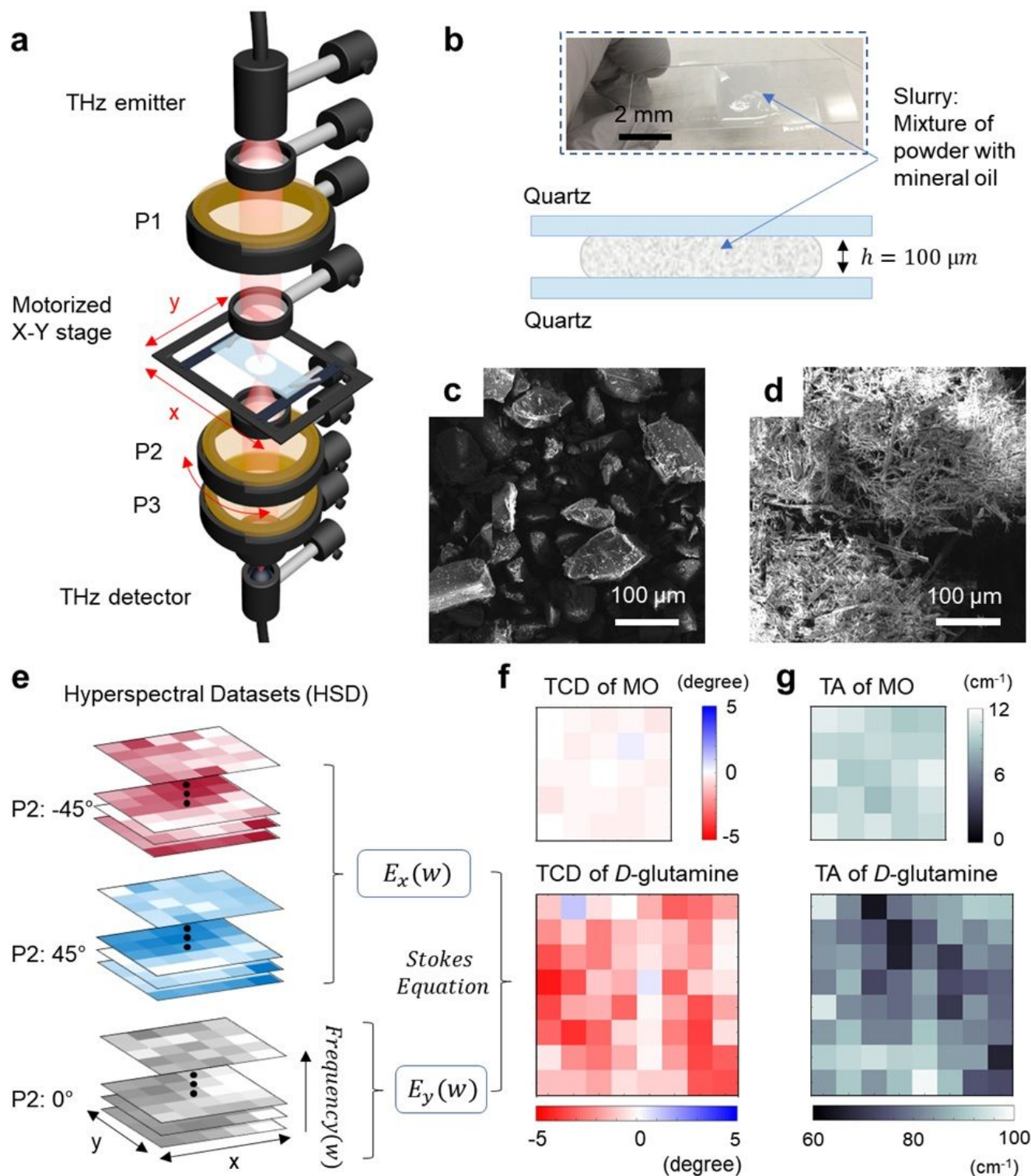


**Figure 1**

Hyperspectral THz-TDP set-up for observation of chiral phonons in AA microcrystals. **a**, Schematics of the THz-TDP setup. Three wire grid polarizers (P1, P2 and P3) were used to analyze polarization states of the beam after passing through the sample. A motorized X-Y stage was used for mapping. **b**, Photograph

and schematic of sandwich quartz cell with slurry mixtures, respectively. c and d, SEM images of before (c) and after (d) recrystallization of L-glutamine. e, Fourier-transformed hyperspectral datasets of electric fields were measured by three different polarization measurements for each pixel. is obtained from the measurements of 45° and -45° for the P2 polarizer and is from 0°, which is along the y direction. f, Example of TCD mapping for reference mineral oil and D-glutamine at 1.69 THz, respectively. g, Example of TA mapping for reference mineral oil and D-glutamine at 1.69 THz, respectively. The size of each pixel in the images of (e-g) is 500  $\mu\text{m}$ .

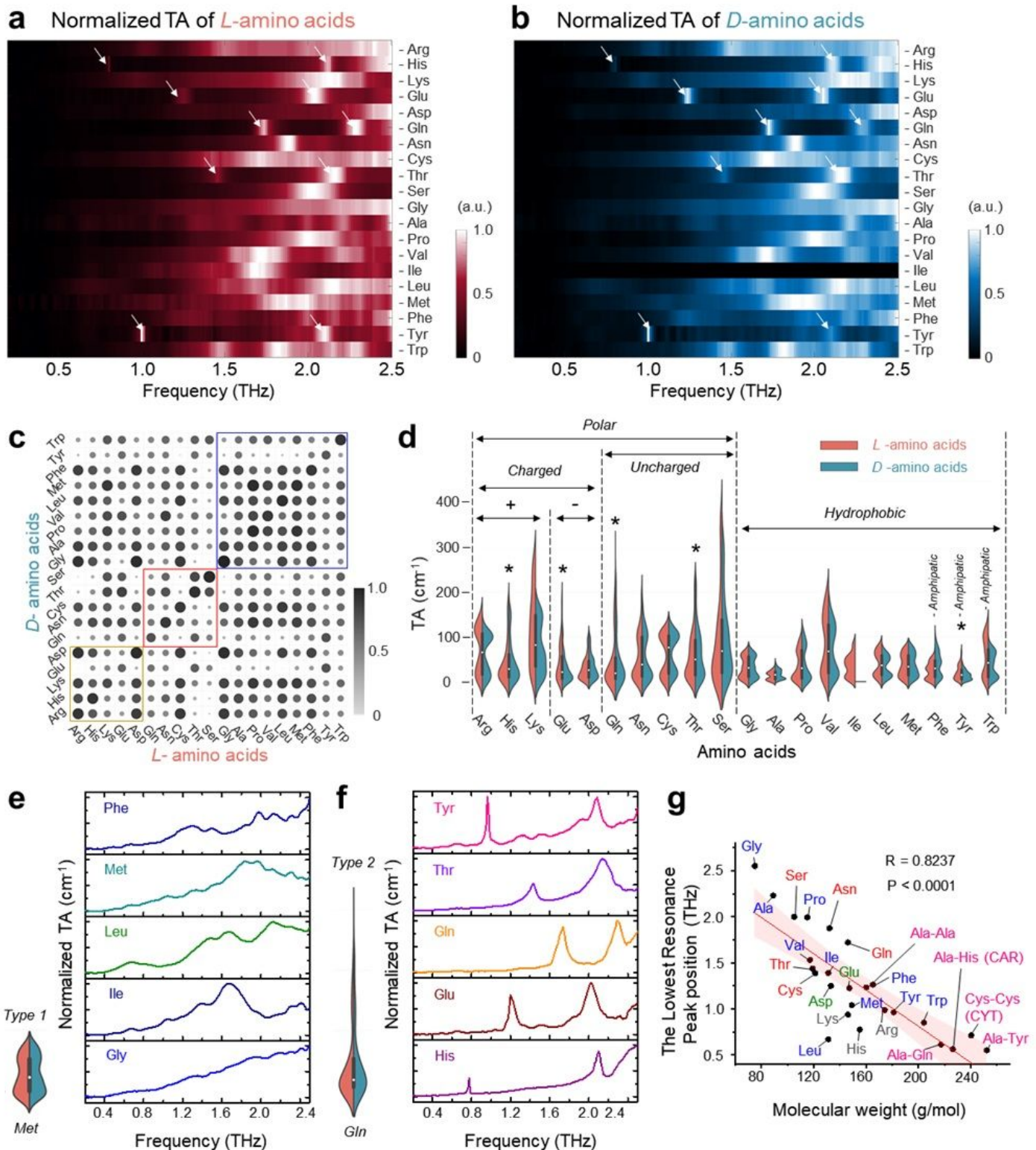


## Figure 2

Analysis of TA spectra for L and D enantiomers of 20 AAs. a and b, 2D plot of TA spectra with band intensity represented by the color brightness. The same samples of achiral glycine were used for the TA analysis. White arrows indicate the appearance of sharp peaks in the spectra. c, 2D correlation matrix between L- and D-AAs without isoleucine. Larger sizes and darker colors indicate higher degrees of similarity between AAs. Some groups show similarity as indicated by square boxes; blue for hydrophobic, red for uncharged polar and gold for charged polar side groups. d, 'Split violin' side-by-side plots for TA spectra of the two enantiomers of AAs. The left half shows those of L-AAs and the right shows those of D-AAs. e and f, Normalized TA spectra of five representative L-AAs having broad peaks and sharp peaks, respectively. The shape of the distribution is dependent on the width of the peaks: broad peak AAs – Type 1, sharp peak AAs – Type 2. g, Molecular weight dependence of the lowest THz resonance peak position. The lowest peak appearing above the baseline was chosen for each AA crystal and the exact peak positions of the absorption peaks are summarized in Table S4. Color labels correspond to different groups; gray - positively charged polar, green - negatively charged polar, red - uncharged polar, blue - hydrophobic AAs and pink - dipeptides. AAs with larger molecular mass show lower resonance frequencies.

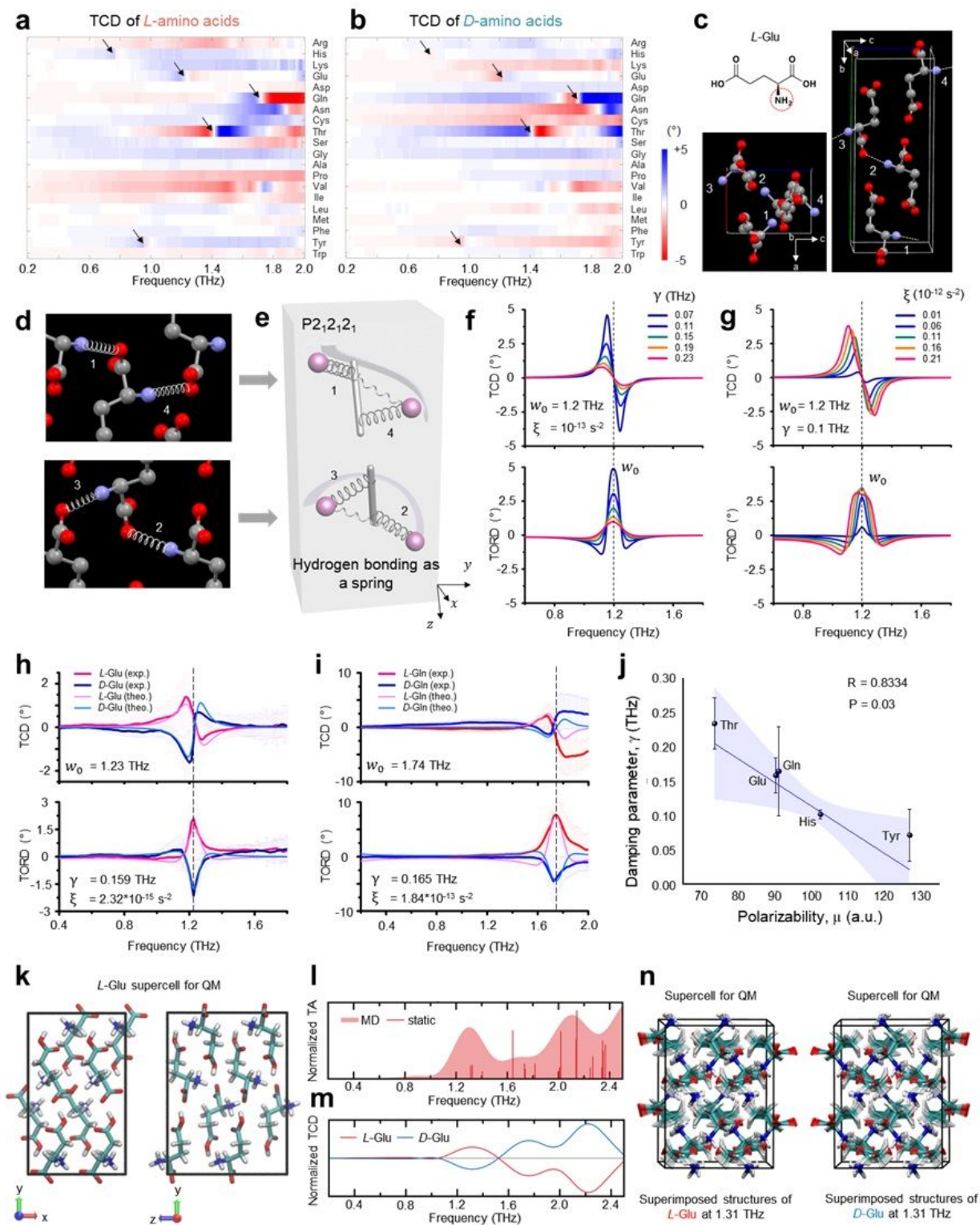


**Figure 3**

Analysis of TCD and TORD spectra for L- and D-enantiomers of 20 AAs. a and b, 2D plot of TCD from 20 proteinogenic L- and D-AAs, respectively. D-isoleucine was not available. The same sample of glycine was used for analysis of both L- and D-AAs. Black arrows indicate crossing zero points corresponding to resonance frequency, from Eq. 1. c, Molecular configuration of *L*-Glu crystal cell as an example of a compound crystallizing in the P212121 space group. Amine groups are helically arranged in the 1-2-3-4

progression. d, Enlarged view of hydrogen bonds in (c), represented as springs in the BK model used for heuristic description of chiral phonons. e, Schematic representation of the unit cell with bi-oscillators in P212121 space symmetry. f and g, TCD and TORD calculated from the BK model varying with damping parameter  $\gamma$  and coupling strength  $\xi$ . h and i, Experimental and calculated TCD and TORD spectra of Glu and Gln, respectively. j, Dependence of  $\gamma$  on the polarizability ( $\mu$ ) of AA molecules<sup>43,44</sup>. k, Supercell of L-Glu used for the QM computations of THz spectra. l, Normalized TA spectra obtained from calculations of the L-Glu supercell in (k) using normal mode analysis (vertical lines) and MD simulations at the QM level (solid surfaces). m, Normalized TCD spectra from the same MD simulations at the QM level used for TA in (l). n, Superimposed structures of the L-Glu molecules along the normal mode (eigenmode) with a frequency of 1.31 THz for the system depicted in (k) (left) and its mirror image (right).

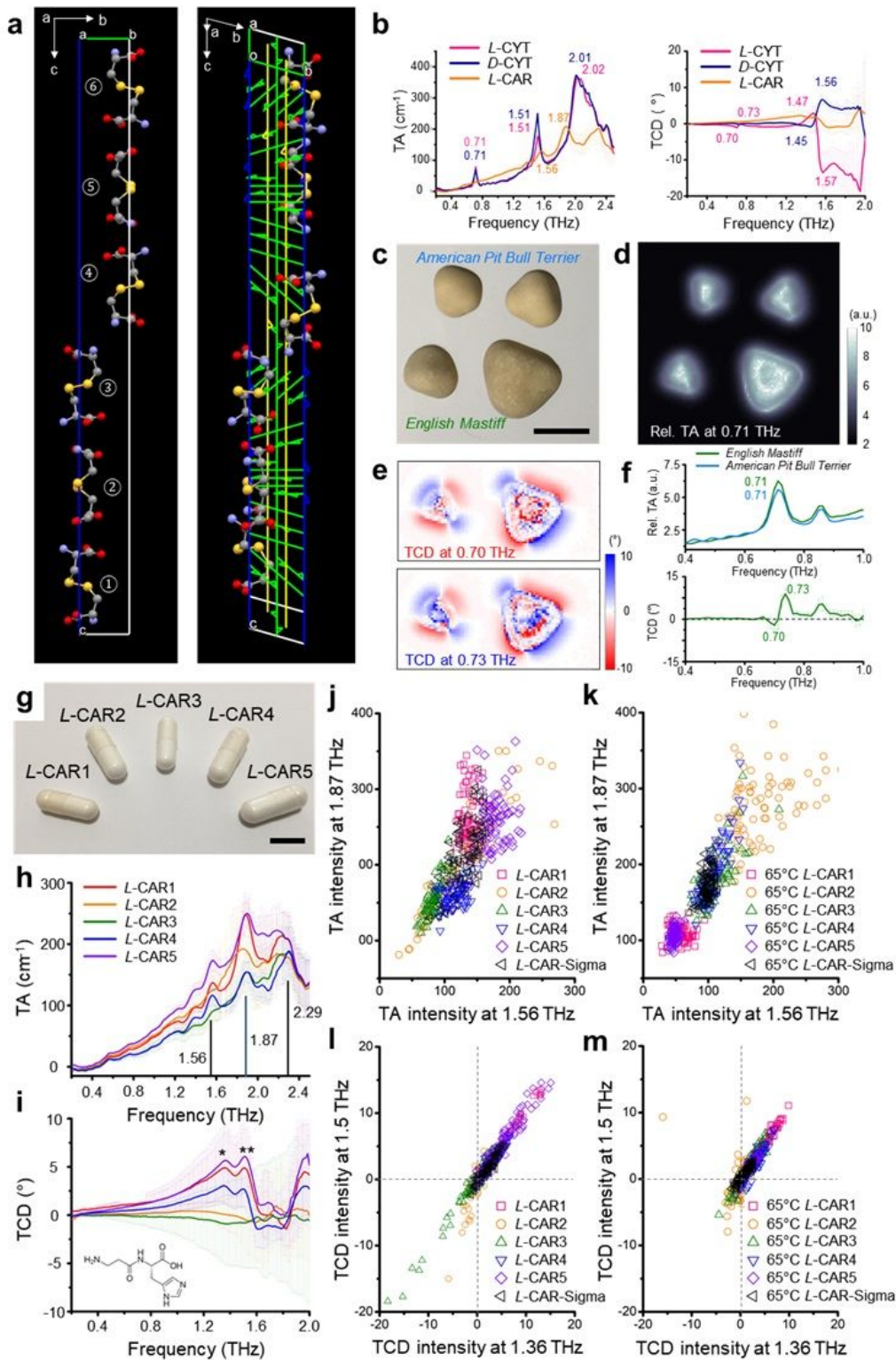


**Figure 4**

Chiral phonons in CYS and CAR. a, Helical axis of L-CYT molecules in a unit cell. Six L-CYT molecules winding a 61 screw axis that coincides with the c-axis as indicated by green helical 'scaffold'. b, Averaged TA and TCD spectra from L-CYT, D-CYT and L-CAR. c, Photograph of four cystine stones from two canine patients. The upper two stones are from a seven-year-old male American pit bull terrier and the lower two stones are from a six-year-old male English mastiff, respectively. Scale bar is 5 mm. d, Relative TA map of

four cystine stones at 0.71 THz. e, TCD map of cystine stones from English mastiff at 0.7 THz and 0.73 THz, respectively. A negative-to-positive transition in the TCD was found in the central part of the stones, while there are birefringence effects in the edges and non-flat areas, indicating variations in the growth conditions and crystallization patterns of the stones. f, Averaged TA and TCD spectra from cystine stones matched well with that of L-CYT crystals prepared in vitro. g, Photograph of five different pills from various manufacturers used for measurements. Scale bar is 1 cm. h and i, Average TA and TCD spectra from as-received L-CAR from five different manufacturers. j and l, 2D peak intensity distribution map of TA and TCD from as-received L-CAR samples. k and m, 2D peak intensity distribution map of TA and TCD from L-CAR slurries after incubation at 65 °C for 48 h.

## Supplementary Files

This is a list of supplementary files associated with this preprint. Click to download.

- [SingleMolecularVibrations.ppt](#)
- [ChiralPhonons.ppt](#)
- [SupplementaryInformationChiralPhonons.docx](#)